Characterization and Far-Field Plume Analysis on the HET-X Hall Effect Thruster

Adrian Vicente[1], Dan Lev[2], and Mitchell Walker[3]
Georgia Institute of Technology, Atlanta, GA, 30318

Nathan Rosenblad[4] and Michael Holmes[5]
Earth Observant Inc., Louisville, CO, 80027

The performance of the Earth Observant Inc. novel 600W Hall effect thruster prototype, designated HET-X, is characterized from 300 W to 1100 W at a facility operating pressure range of 7×10^{-6} to 5×10^{-7} Torr on xenon gas. The performance characterization includes time-resolved measurements of the discharge current oscillations during IVB mapping. A Faraday probe and retarding potential analyzer were used to measure the ion current density profile from $-90°$ to $+90°$ and the ion energy distribution function, respectively. The calculated beam divergence half angle was $22.5°$, and current utilization and voltage utilization efficiencies are 92.4% and 93.6% respectively. The thruster achieves a maximum performance of 38.7% efficiency at a maximum I_{sp} of 1576 s. The maximum *T*/*P* ratio is 70.2 mN/kW.

Nomenclature

A_C	=	Probe cross-sectional geometric area, m^2
e	=	Elementary charge; $1.602 \times 10^{-19} C$
$f(E_i/q_i)$	=	Ion energy per unit charge distribution function
$f(u_i)$	=	Ion velocity distribution function
$f(x_j)$	=	Smoothing algorithm output function
g	=	Gravitational acceleration; 9.807 m/s^2
h_C	=	Height of Faraday probe collector, m
h_{GR}	=	Height of Faraday probe guard ring, m
I_A	=	Axial beam current, A
I_B	=	Beam Current, A
I_D	=	Discharge current, A
$I_{D,RMS}$	=	Peak-to-Peak discharge current, A
I_C	=	Current measured by RPA probe collector, A
I_{FP}	=	Current measured by Faraday probe collector, A
I_K	=	Cathode keeper current, A
$I_{M,i}$	=	Inner magnet coil current, A
$I_{M,o}$	=	Outer magnet coil current, A
I_{sp}	=	Specific impulse, s
j	=	Ion current density, A/m^2
$\dot{m}_a$	=	Anode mass flow rate, mg/s
$\dot{m}_c$	=	Cathode mass flow rate, mg/s
$\dot{m}$	=	Total mass flow rate, mg/s
n_i	=	Ion number density, $1/m^3$
P	=	Total thruster power, W

1 PhD Candidate, Daniel Guggenheim School of Aerospace Engineering, 625 Lambert St NW
2 Research Engineer, Daniel Guggenheim School of Aerospace Engineering, 625 Lambert St NW
3 Lab Director, Daniel Guggenheim School of Aerospace Engineering, 625 Lambert St NW
4 Chief Engineer, 280 S Taylor Ave., Unit 200
5 Director of Propulsion, 280 S Taylor Ave., Unit 200

p	=	Smoothing parameter
q_i	=	Ion charge number
R_C	=	Radius of Faraday probe collector, m
R_{GR}	=	Radius of Faraday probe guard ring, m
T	=	Thrust, N
u_i	=	Ion velocity, m/s
V_a	=	Anode voltage, V
V_b	=	Thruster body voltage, V
V_D	=	Discharge voltage, V
V_K	=	Cathode keeper voltage, V
$V_{M,i}$	=	Inner magnet coil voltage, V
$V_{M,o}$	=	Outer magnet coil voltage, V
V_{RPA}	=	Most-probable ion energy per charge voltage, V
V_3	=	RPA retarding grid voltage, V
x_j	=	Smoothing algorithm independent variable
y_j	=	Smoothing algorithm dependent variable
α_m	=	Mass utilization correction due to charge state
Γ_k	=	Particle flux of the *k*th species, $1/m^2 s$
γ_k	=	Secondary electron emission yield of the *k*th species, $electrons/ion$
Z_k	=	Ion charge state of the *k*th specie
η	=	Thruster total efficiency
η_a	=	Thruster anode efficiency
η_v	=	Thruster voltage utilization efficiency
η_d	=	Thruster divergence efficiency
η_m	=	Mass utilization efficiency
η_q	=	Charge utilization efficiency
θ	=	Angular coordinate, °
κ_A	=	Correction for ion angle of incidence
κ_D	=	Correction for probe distance to thruster
κ_G	=	Correction for probe ion collection area
κ_{SEE}	=	Correction for collector secondary electron emission
λ	=	Far-field divergence half-angle, °
Ω_k	=	Ion current fraction of the *k*th species

I. Introduction

Space electric propulsion (EP) is a branch of in-space propulsive technology. EP serves an attractive alternative to chemical propulsion due to its high specific impulse (I_{sp}) and fuel efficiency. Many technologies exist under the umbrella of EP, each of which varies in the particular mechanism by which they ionize their propellant and accelerate it from the spacecraft. The Hall effect thruster (HET) is one such thruster that uses magnetic and electrostatic fields to ionize and accelerate its propellant. Compared to other EP technologies, HETs boast greater thrust output and thrust efficiency at high power levels. As such, research and development of HETs have increased significantly in recent years, and there is growing interest in HETs for orbit-raising, deep-space, and very low Earth orbit (VLEO) applications [1].

Earth Observant Inc. (EOI) has developed a HET for application to small satellites in VLEO. The small form factor of the thruster prototype, designated HET-X, seeks to address several challenges relating to HET use for small-satellite architectures. Georgia Tech performed a preliminary characterization of HET-X to determine the relative benefits of its unique design features. Characterization of the HET-X thruster, performed at the High-Power Electric Propulsion Lab (HPEPL), was broken down into two phases of experimentation. During the first phase, the performance is characterized to identify thruster configurations that yield the maximum I_{sp} and maximum thrust-to-power ratio (T/P). This was prefaced with IVB mapping to refine the survey. During the second phase, the far-field

plasma plume is characterized to quantify the plume divergence angle, current utilization, and voltage utilization efficiencies.

II. Experimental Setup

A. Vacuum Facility

The HET-X thruster was tested in the VTF-2 (Vacuum Test Facility 2) chamber at HPEPL [2]. The chamber is cylindrical, measuring approximately 9 m in length and 5 m in diameter. The chamber achieves a rough vacuum of 30 mTorr using a 3800 CFM blower and a 495 CFM rotary-vane pump. To reach high-vacuum, the facility employs ten CVI TMI reentrant (nude) cryopumps that give the facility a nominal pumping speed of 350,000 l/s on xenon. Chamber pressure during thruster operation varied from 7×10^{-6} to 5×10^{-7} Torr, with a measurement uncertainty of $\pm 10\%$. Pressure measurements were captured using two Agilent 571 Bayard-Alpert ion gauges. One gauge was located at the chamber wall, while the other was positioned 1.0 m adjacent to the thruster. The chamber contains a downstream graphite-shielded beam dump.

B. Thruster

HET-X was designed and constructed by EOI (Earth Observant Inc.). It was built with the intent of developing a high power density, propellant-agnostic HET within a small form factor. The thruster was optimized for 600-W operation but is capable of sustained operation in excess of 1 kW. It was tested on 99.9995% purity xenon and utilized a 50/50 water-glycol mixture for liquid cooling. The propellant flow was regulated using MKS GE50A flowmeters. The flowmeters were calibrated using a MesaLabs DryCal-800, providing a flow rate uncertainty of $\pm 0.15\%$. Time-resolved measurements of thruster biases were captured using a Teledyne LeCroy HDO 6104 oscilloscope. V_a and V_b were measured with respect to facility ground using CT4024 probes, providing measurement uncertainty of ±3%. Cathode potential with respect to facility ground was measured using a PP018 probe, with an accuracy of ±1%. The thruster discharge current was measured using a CP150 probe with an uncertainty of ±1%. All measurements were recorded simultaneously, in addition to a measurement of the power spectrum of the discharge current. The thruster is operated continuously for a minimum of four hours before performing measurements. The thruster is operated for a minimum of five minutes at each new operating condition before performing measurements.

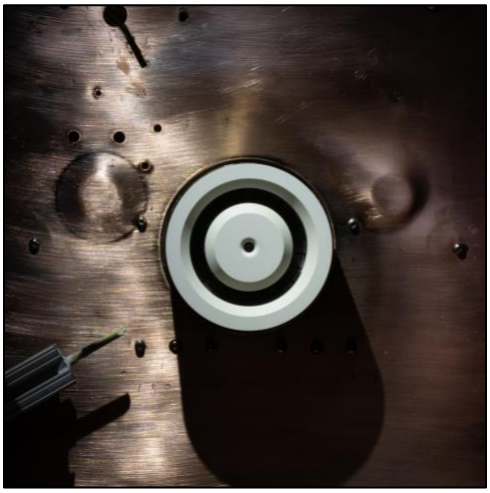

Figure 1. *Image of the HET-X Thruster*

C. Thrust Stand

Thrust was measured using the null-type, inverted pendulum thrust stand [3]. It is mechanically comprised of a stationary lower stage and a traveling upper stage, which are connected using parallel linkages. The thruster is mounted upon the upper stage. During operation, the position of the upper plate is measured using a linear voltage differential transformer (LVDT) and is controlled using two electromagnetic actuators. The current through each actuator is controlled using a pair of Stanford Research Systems SIM960 PID control loops, which use the LVDT signal as the input and then modulate the output current through the actuators. One actuator is dedicated to the cancellation of vibrational noise (damper coil), while the other holds the upper plate stationary (null coil). A low-pass filter at the PID

control input attenuates high-frequency vibrations. The null coil current is required to maintain the initial position of the thrust stand thrust. The thrust stand was calibrated for a measurement range of 0 to 230 mN and demonstrated an uncertainty of ±5%. The thrust stand was calibrated prior to measurement at every setpoint.

D. Faraday Probe

A Faraday probe is employed to measure the ion current density profile of the HET [4]. The JPL-style Faraday probe is composed of a circular collector with an outer diameter of 22 mm. The collector has a tungsten spray coating to reduce secondary electron emission and is encompassed by a guard ring. The normal of the collector face is aligned along the thruster axis when positioned 1.0 m downstream of the thruster exit face. The probe was swept on an azimuthal motion stage from -90° to +90° from the thruster centerline in steps of 0.085°. The collector and guard ring were both biased to -30 V to repel electrons whilst keeping sheath expansion negligible. Current through the probe collector was obtained by measuring the voltage drop over a 1Ω shunt using an Agilent 34980A, providing a measurement uncertainty of ±0.004%.

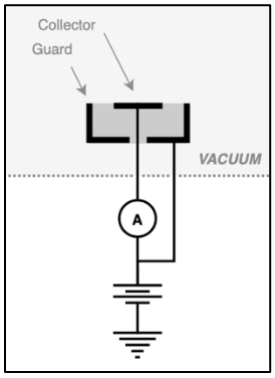

Figure 2. *Electrical schematic of the Faraday probe.*

E. RPA

We employ an AFRL-style Retarding Potential Analyzer (RPA) to measure the ion energy per charge distribution function [5]. The RPA is rotated on an azimuthal motion stage from -90° to +90° from the thruster centerline in steps of 45°. The ion-retarding grid bias was swept from 0 to 150% of the HET discharge voltage in steps of 1 V with a Keithley 2410 Sourcemeter. The collector current is measured using a Keithley 6487 Picoammeter, with a measurement uncertainty of ±0.2%.

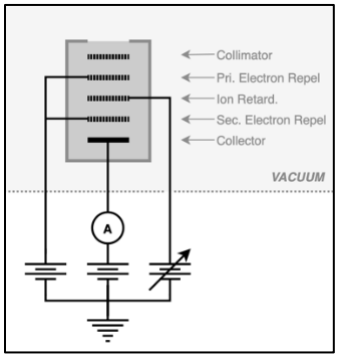

Figure 3. *Electrical schematic of the RPA probe.*

III. Results

The objective of the first phase of the investigation is to identify the thruster operating conditions that generate maximum I_{sp} and T/P ratio. We use the IVB map to identify the stable operating points.

A. IVB Mapping

A current-voltage-magnetic field (IVB) map is a tool that visualizes and identifies regions of HET stability. It is created by plotting a 3D contour plot of RMS discharge current $I_{D,RMS}$ as a function of discharge voltage V_D and magnet current $I_{M,i}$. There are many variations on the IVB map, such as by plotting normalized B-field instead of magnet current or peak-to-peak discharge current instead of RMS [6], but the analysis is ultimately analogous. Similar to a performance survey, IVB mapping requires empirical testing of the thruster. However, it can greatly narrow the range of inputs considered in a performance survey by identifying a *"basis configuration."*

To create the IVB map, the HET outer-to-inner coil current ratio $I_{M,o}/I_{M,i}$, cathode-to-anode flow rate ratio $\dot{m}_c/\dot{m}_a$, anode flow rate $\dot{m}_a$, and cathode inputs remain constant. The maps are performed at various anode flow rates. Once these values are set, a range of discharge voltages V_D and magnet currents $I_{B,i}$ must be selected. The HET is operated at each test point, while the resulting RMS discharge current $I_{D,RMS}$ is measured. The results are presented in a 3D contour plot and analyzed for regions of thruster stability. Typically, IVB maps show that the $I_{D,RMS}$ is minimized at the lower V_D and $I_{M,i}$ and is maximized at higher V_D and $I_{M,i}$. The regions of low and high $I_{D,RMS}$ are referred to as the stable region and unstable region, respectively. Because higher values of $I_{D,RMS}$ are associated with thruster instability, a viable HET operating point is found in the stable region. By identifying this V_D (and its associated $I_{M,i}$), the experimenter has also found the *"basis configuration"* for their performance survey.

In this study, two IVB maps are performed at anode flow rates of 1.5 and 3.9 mg/s. Mapping was constrained to an $I_{M,o}/I_{M,i}$ of 0.4 and an $\dot{m}_c/\dot{m}_a$ of 0.1. The selected V_D range was 150 V to 300 V in steps of 50 V, while the $I_{B,i}$ range was 1 A to 2.5 A in steps of 0.5 A. IVB maps are normally conducted at much higher resolutions than are presented here [7].

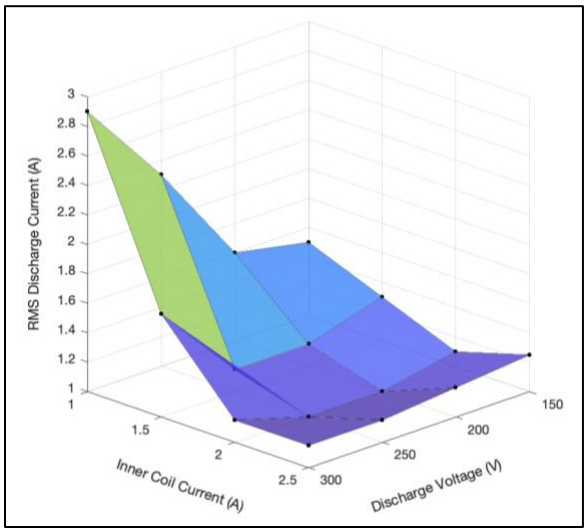

Figure 5. *IVB Map, anode flowrate 1.5 mg/s*

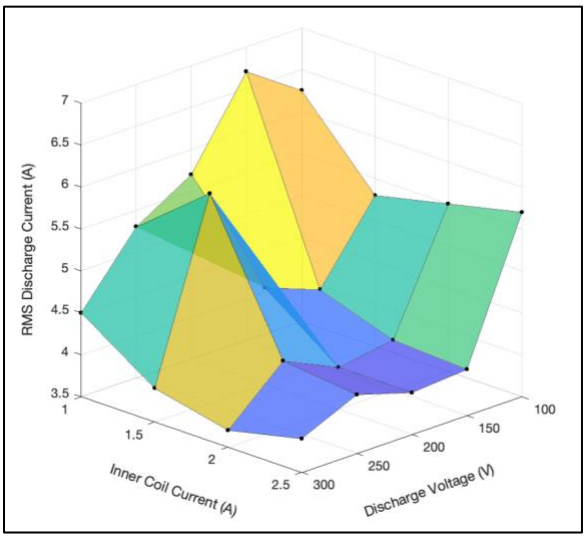

Figure 6. *IVB Map, anode flowrate 3.9 mg/s*

The unstable region was not captured in either IVB map. However, the stable region and transition were captured, which are all that are needed to identify the *"basis configuration."* The IVB map for the 1.5 mg/s flow rate demonstrated a smooth transition to instability. The $I_{D,RMS}$ was shown to consistently increase as the V_D. A minimum $I_{D,RMS}$ of 1.0 A was seen at several points. Because of its proximity to the $I_{D,RMS}$ transition, the 250 V and 1.5 A setpoint was selected as the "*basis configuration"* for this flow rate. The IVB map for the 3.9 mg/s flow rate demonstrated several peaks of severe instability, even at relatively low V_D. The minimum $I_{D,RMS}$ measured for this map was 3.7 A, which was seen at several configurations. Due to the lack of adjacent peaks in instability, the 150 V and 2 A setpoint was selected as the *"basis configuration"* for this flow rate.

B. Performance Characterization

Having identified *"basis configuration,"* a performance survey was conducted in which all thruster inputs were independently varied in search of optimal configurations that would yield maximum I_{sp} and T/P. Thrust, electrical power consumption, and propellant mass flow rate were measured for all setpoints to compute these values as outlined in (i) through (iv). The thruster inputs and resulting performance metrics are outlined below in Table 1.

$$P = I_D V_D + I_{M,i} V_{M,i} + I_{M,o} V_{M,o} + I_K V_K \tag{i}$$

$$\dot{m} = \dot{m}_a + \dot{m}_c \tag{ii}$$

$$I_{sp} = \frac{T}{\dot{m} g} \tag{iii}$$

$$\eta = \frac{T^2}{2\dot{m}P} \tag{iv}$$

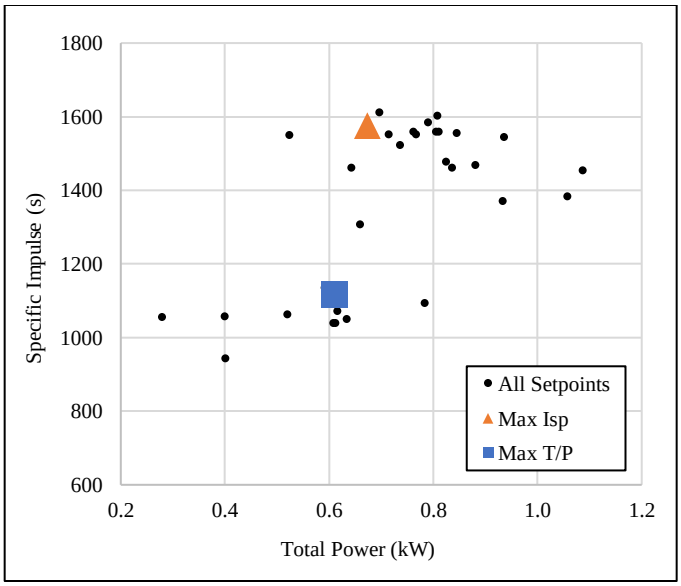

Figure 7. *HET I_{sp} vs P*

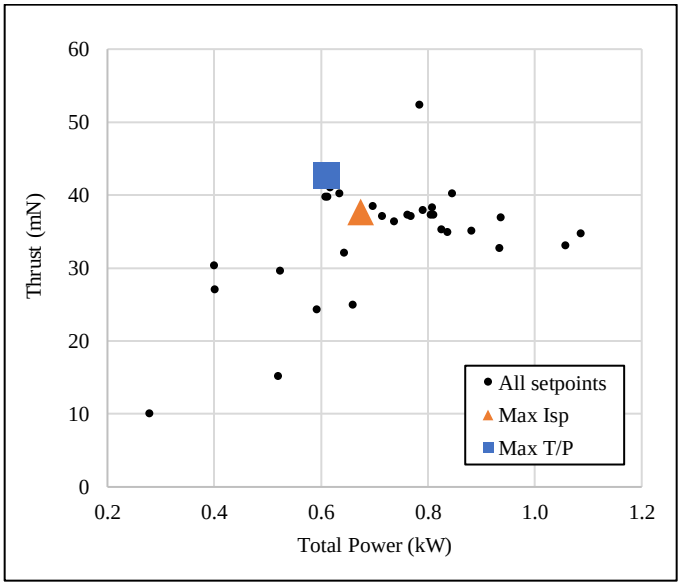

Figure 8. *HET-X Setpoint Survey, T vs P*

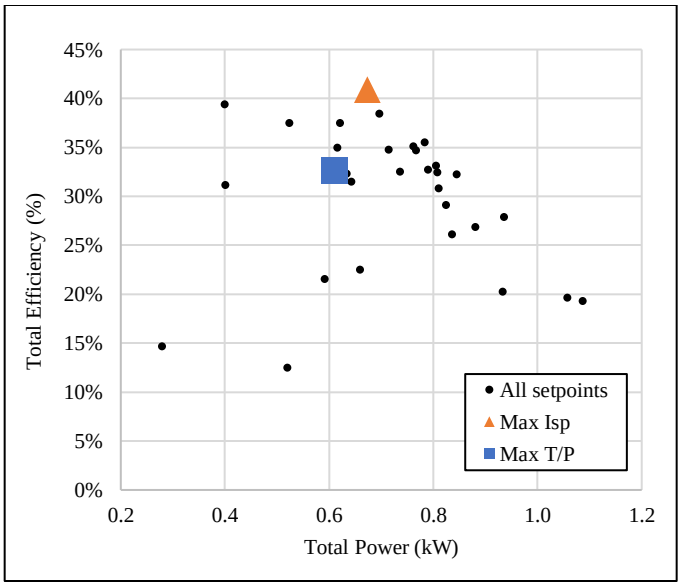

Figure 9. *HET-X Setpoint Survey, η vs P*

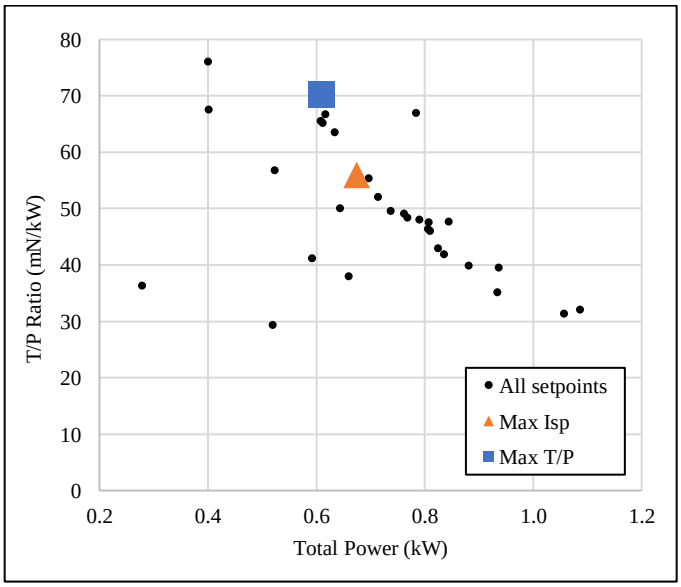

Figure 10. *HET-X Setpoint Survey,T/P vs P*

Over 30 configurations were tested and are illustrated in Figures 7 through 10. The optimal configurations that yielded maximum I_{sp} and T/P ratio are also outlined in these figures. Table 1 contains the thruster inputs for each operating point, and Table 2 contains the measured performance metrics.

For phase two, the far-field plume of the two operating points was characterized with Langmuir, Faraday, and RPA probes. The purpose of this was to characterize thruster performance due to individual physical processes. The relation (iv) is a means of succinctly calculating the total thruster efficiency. However, it doesn't provide much context on what specific elements of the thruster may be underperforming and bringing down the overall efficiency. For this reason, it is desirable to use a phenomenological model, which decomposes and describes the various physical phenomena that affect the overall efficiency of the HET. Many such models exist, one of which is described below in (v) through (x) [8][9].

$$\eta_a = \eta_v \eta_d \eta_b \eta_m \eta_q \qquad (v)$$

$$\eta_v = \frac{V_{RPA}}{V_D} \tag{vi}$$

$$\eta_d = (\cos(\lambda))^2 \tag{vii}$$

$$\eta_b = \frac{I_B}{I_D} \tag{viii}$$

$$\eta_m = \frac{(\dot{m}I_B)}{(\dot{m}_a e)}\alpha_m \quad ; \quad \alpha_m = \sum_k \frac{\Omega_k}{Z_k} \tag{ix}$$

$$\eta_q = \frac{\left(\sum_k \Omega_k/\sqrt{Z_k}\right)^2}{\sum_k \Omega_k/\sqrt{Z_k}} \tag{x}$$

The thruster anode efficiency η_a is the same as the total efficiency calculated in equation (iv). The voltage utilization efficiency η_v describes how much of the voltage provided by the discharge supply is actually used to accelerate the ions. Divergence efficiency η_d describes how much of the kinetic energy imparted to the ion is axial and thus produces thrust. The current utilization efficiency (or beam current efficiency) η_b describes how much of the discharge current is carried by ions instead of electrons, as electrons generate negligible thrust. The mass utilization efficiency η_m describes how much of the propellant is ionized before exiting the thruster channel. The charge utilization efficiency η_q is comprised of various terms that describe the effects of multiply-charged ions that are not already addressed in the other efficiency terms.

The measurements required to calculate divergence and current utilization may be performed with a Faraday probe. Measurements required for voltage utilization may be performed using an RPA. Mass utilization is computed from Faraday and ExB probe measurements. Charge utilization also requires ExB probe measurements. Due to time constraints, measurements with the ExB probe could not be performed. Thus, only divergence, current utilization, and voltage utilization efficiencies will be presented in this paper. These will serve to identify some potential underperforming mechanisms of the HET-X's operation and drive future development.

C. Noise Reduction

To reduce the noise measured by the far-field probes, a cubic smoothing spline was used for all the probe current measurements. Cubic smoothing spline interpolation is a curve-fitting technique in which the resulting function f minimizes the expression (*xi*).

$$\min\left\{ p\sum_{j=1}^{n}\left|y_j - f(x_j)\right|^2 + (1-p)\int |f''|^2 dx \right\} \tag{xi}$$

Here, x_j is to the input variable, y_j is to the output variable, and f is the smoothed output. The cubic smoothing spline is bound by two functional constraints: one minimizes the squared error between the data and the spline, and the second minimizes the curvature. These are represented by the left and right terms of (xi), respectively. The relative importance of each term is determined by the smoothing parameter p, which is selected as some value between 1 and 0. If $p = 1$, the output f passes through all data points, resulting in an interpolation spline. If $p = 0$, only the curvature is minimized, resulting in a linear least squares fit of the dataset. A smoothing parameter of 0.1 was selected to reduce the noise in all probe data, resulting in smoothing seen in Figures 11 and 12. Algorithms for computing cubic smoothing splines are available in the literature [10] and are also included in many programming platforms.

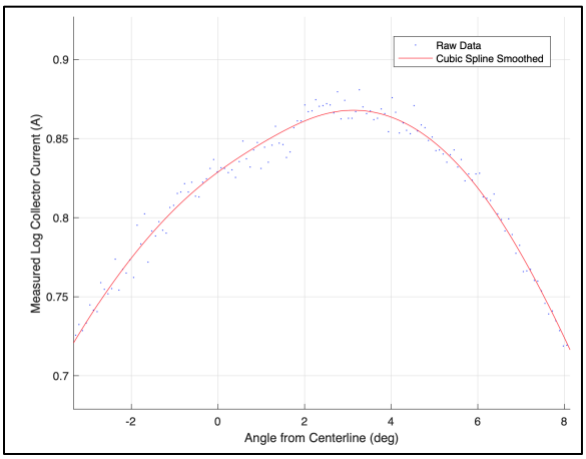

Figure 11. *Detail of data smoothing for Faraday probe*

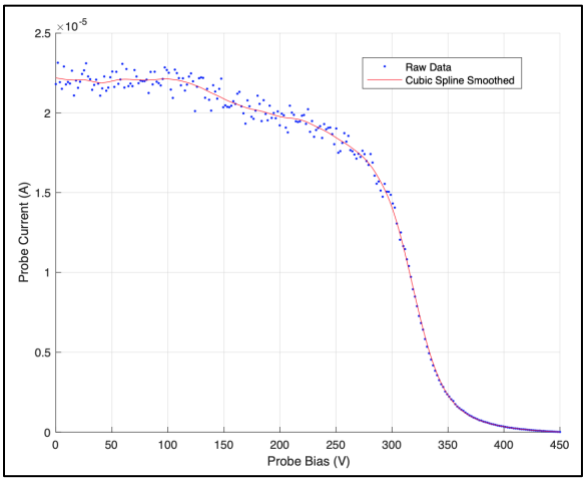

Figure 12. *Data smoothing for RPA probe*

D. Faraday Probe

Ion current density was captured with the Faraday Probe using the methodology outlined in Brown et al [4]. Since the probe was used on an azimuthal motion stage, which utilizes a hemispherical coordinate system, ion current density is calculated using (xii).

$$j = \sum \Gamma_k Z_k e = \frac{I_{FP}}{A_C + \kappa_G} \kappa_{SEE} \tag{xii}$$

In which I_{FP} is the measured probe collector current, A_c is the geometric area of the collector face, κ_{SEE} is a correction for secondary electron emission (SEE) at the collector surface, and κ_G is a correction for ions collected in the gap between the collector and the guard ring.

$$\kappa_G = \pi(R_{GR}^2 - R_c^2)\left(\frac{2\pi R_C h_C}{2\pi R_C h_C + 2\pi R_{GR} h_{GR}}\right) \tag{xiii}$$

$$\kappa_{SEE} = \frac{1}{1 + \sum_k \frac{\Omega_k \gamma_k}{Z_k}} \tag{xiv}$$

The κ_G correction accounts for the effective cross-sectional collector area, which is slightly larger than A_C due to the plasma sheath that extends from the body. The effect of the sheath is largely negated by the presence of the guard ring, but there is still a nonnegligible amount of current that enters the gap between them. For this, it's been shown that the ratio of ions collected by the collector vs the guard ring is proportional to the ratio of the exposed gap area. The terms R_C, R_{GR}, h_C, and h_{GR} all refer to Faraday probe dimensions.

The κ_{SEE} correction accounts for the additional current generated by SEE from the collector due to impacting ions. Here, Ω_k is the ion current fraction of the kth species, Z_k is the charge state of the kth species, and γ_k is the SEE yield of a material due to the kth species. In HET analysis, only the +1, +2, and +3 ionized species are considered. The presence of higher charge species is negligible. The SEE yields for tungsten are referenced from the literature [11], and the ion current fractions are estimated to be the same as another HET with similar discharge conditions [12].

Finally, a correction for ions created from charge-exchange collision (CEX) must be applied to the entire probe trace. The Faraday probe is intended to capture the current carried by thruster-generated ions. However, it cannot distinguish between these and CEX ions. CEX ions are slow-moving, so their motion is greatly influenced by the radial electric field of the plume in the far-field. Because of this, CEX ions are trajected in all directions and collected by the Faraday probe in places where thruster-generated ions are not present. The consequence of this is a broadening of the plume periphery beyond $\pm 40°$ from the centerline and increased overall divergence of the plasma plume. The optimal way to correct for this effect is to take probe traces at multiple facility background pressures, perform a linear regression of ion current density, and extrapolate to zero pressure. In lieu of that, an estimate correction may be applied by taring the entire trace such that the ion current density is zero at $\pm 90°$. Due to time constraints, the latter was done.

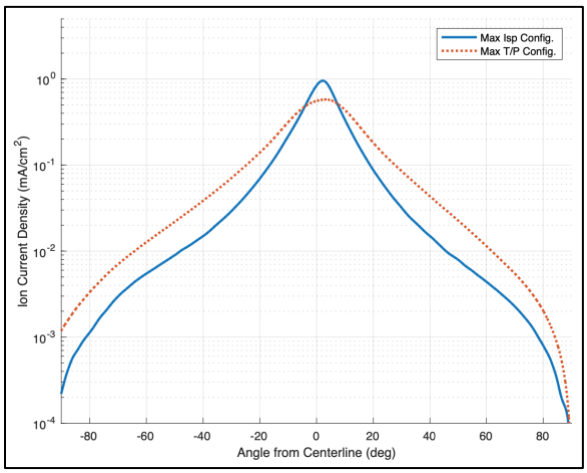

Figure 13. *Ion current density at 1.0 m from thruster face*

$$I_B = 2\pi R^2 \int_0^{\pi/2} j[\theta] \frac{\kappa_D}{\kappa_A} \sin(\theta)\, d\theta \qquad (xv)$$

$$I_A = 2\pi R^2 \int_0^{\pi/2} j[\theta] \frac{\kappa_D}{\kappa_A} \cos(\alpha_A)\sin(\theta)\, d\theta \qquad (xvi)$$

$$\lambda = \cos^{-1}(I_A/I_B) \qquad (xvii)$$

Figure 13 illustrates the faraday traces conducted for the max I_{sp} and the max T/P configurations, plotting the ion current density as a function of azimuthal angle. Both traces demonstrate a peak slightly right of the motion-stage center. This is due to off-center mounting of the thruster, and is not indicative of thruster malfunction. The max I_{sp} configuration has a beam efficiency of 92.4%, a half angle divergence of 22.5 degrees, and a resulting divergence efficiency of 85.4%. Relative to this, the max T/P configuration underperforms with a beam efficiency of 89.5%, a half-angle divergence of 26.3 deg, and a divergence efficiency of 80.0%. As HET efficiency generally improves with increased voltage, this is not especially surprising. Relative to similar thrusters, the beam efficiency for both

configurations is high, while the divergence efficiency is comparably low [9]. These metrics are summarized below in Table 2.

E. RPA Probe

The RPA probe measures ion energy per charge by filtering the downstream plasma plume through four independently biased grids. The primary operation is performed by the third grid, the ion-retarding grid, which selectively filters ions from the plume. This grid decelerates incoming ions through the adverse electric field that it generates. Effectively, this grid acts as a high-pass filter that only allows ions with higher energy than the retarding grid to pass through to the collector. By increasing the voltage on this grid, ions with equal or less energy are repelled, and the collected current drops. The retarding grid bias is typically varied from 0 to ~120% of the thruster discharge bias V_D, with collector current measured at every step in bias.

Analysis of the RPA trace yields the ion energy distribution function. For this, two assumptions must be made. First, that ion motion is unidirectional, which is approximately the case for ion accelerated from a HET. Second, the energy of the ions is comprised entirely of its kinetic energy. In doing this, we can implement the expression for the velocity distribution function (xviii). Ultimately, we may arrive at an expression for the ion energy distribution function per unit charge $f(E_i/q_i)$ (xix), the derivation for which may be found in the literature [13]. Here, A_c is the collector area, m_i is the ion mass, q_i is the ion charge, n_i is ion number density, and dI_C/dV_3 is the derivative of collector current with respect to grid voltage.

$$I_C(V_3) = A_C q_i e n_i \int_{u_{\min(V)}}^{\infty} u_i f(u_i)\ du_i \qquad (xviii)$$

$$f(E_i/q_i) = -\left(\frac{m_i}{A_C q_i^2 e^2 n_i}\right)\frac{dI_C}{dV_3} \qquad (xix)$$

$$f(E_i/q_i) \propto -\frac{dI_C}{dV_3} \qquad (xx)$$

What is important for us to quantitatively extract is the grid voltage V_3 which generates the most-probable ion energy. This votlage, V_{RPA}, is the value where $f(E_i/q_i)$ maximizes. When it comes to HET performance characterization, this peak is generally all that interests us. Further, because $f(E_i/q_i)$ is proportional to $-dI_C/dV_3$, it is unnecessary for us to compute the exact values of the distribution function. The peak can be identified just as easily by plotting and maximizing $-dI_C/dV_3$ instead, which is why this is commonly done [14,15].

Ideally, if the HET anode is biased to a given voltage, then all thruster-generated ions will be accelerated to that energy. If our discharge bias V_D is, for instance, 300V, we would find that our most-probable ion energy per charge V_{RPA} would be 300V as well. However, the ions' kinetic energy at the thruster exit will always be less than the acceleration potential. Since ionization occurs within a wide region of the discharge channel, the ion velocity upon acceleration is variable and so is the ion kinetic energy. Further, these ions are also influenced by the electric fields generated locally in different parts of the discharge channel and plume. These losses in ion acceleration are quantified in voltage utilization efficiency η_v, which directly compares measured V_{RPA} to V_D.

RPA analysis was carried out at 0°, 45°, and 90° from the thruster centerline. The RPA trace was smoothed, the derivate of the collected current I_c with respect to V_3 was computed, and the negative was plotted with respect to V_3. The value of V_{RPA} was identified in each plot for the centerline position.

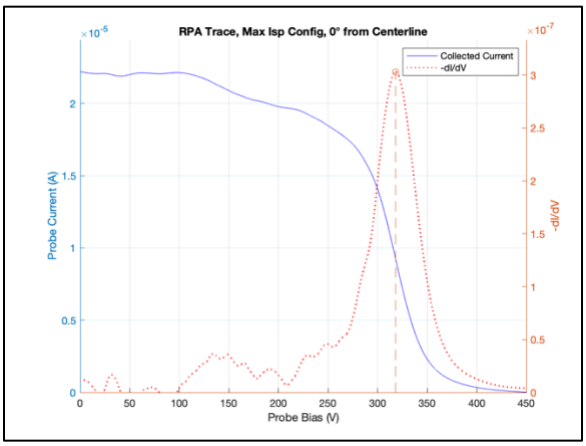

Figure 14. *RPA trace of max I_{sp} config. at 0° from centerline*

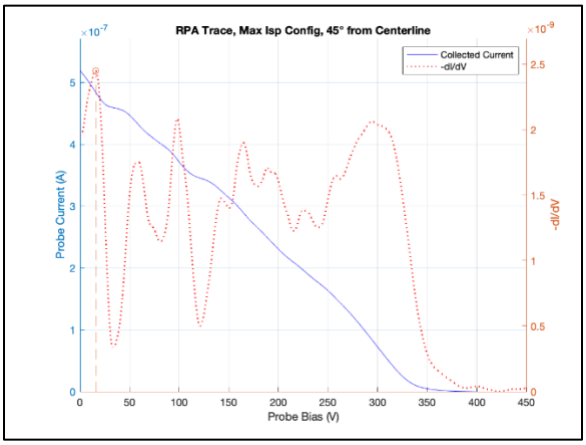

Figure 15. *RPA trace of max I_{sp} config. at 45° from centerline*

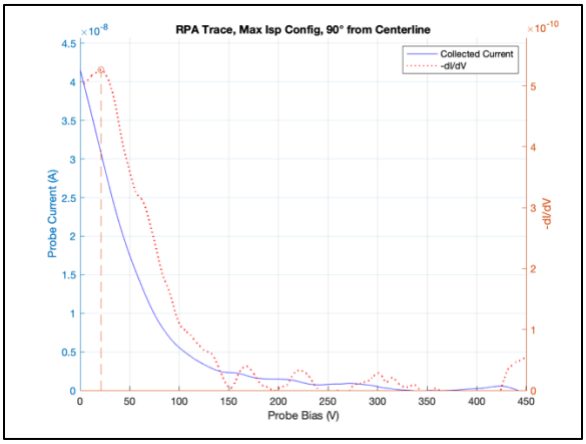

Figure 16. *RPA trace of max I_{sp} config. at 90° from centerline*

The centerline RPA trace for the max I_{sp} configuration yields a distinct and narrow peak at 318V. Voltage utilization efficiency is calculated as 93.6%. There is a series of small peaks leading up to the most-probable peak, which may be attributed to stochastic noise. These peaks might be eliminated by increasing the smoothing parameter, but it would be preferable to increase the number of samples/traces. This might also be improved by increasing the energy resolution. However, time constraints did not allow for either. The traces taken at 45° and 90° from the centerline illustrate how the most-probable voltage decreased as the probe was moved progressively further from the centerline.

The traces appear to be much more noisy than the centerline, and it initially appears difficult to extract much useful data from them. However, we note two important observations. Firstly, the measured current I_C for these two traces is more than two orders of magnitude smaller than that collected at the centerline. Second, the most prevalent peaks occur at low energies, indicating a very slow speed. The 45° trace demonstrates an absolute maximum peak at 19 V, but illustrates a wide spread of ions with energies spread between 0 and 300 V. The 90° trace demonstrates a distinct peak at 21 V. We may assume that these demonstrate large fractions of CEX and elastic collisional ions. Thus, we assert that the vast majority of thruster-generated ions are found within a divergence half-angle of less than 45°. This is reinforced by our Faraday traces and the calculated divergence efficiency.

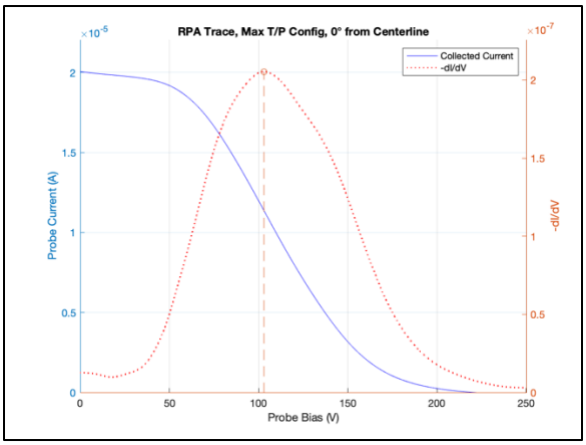

Figure 17. *RPA trace of max T/P config. at* 0° *from centerline*

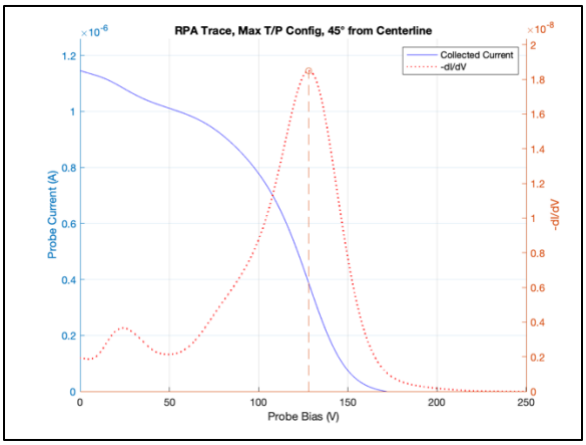

Figure 18. *RPA trace of max T/P config. at* 45° *from centerline*

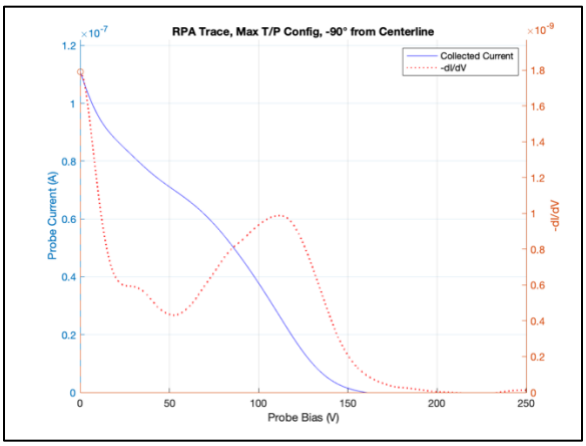

Figure 19. *RPA trace of max T/P config. at* 90° *from centerline*

The centerline RPA trace for the max T/P configuration yields a distinct peak at 103V, but it is much broader than the trace for max I_{sp}. This increased broadness was unexpected, as the max T/P configuration utilizes a lower discharge voltage. High discharge voltage typically results in increased energy distribution and thus a larger spread in possible ion energies [13]. What was even more unexpected was the trace taken at 45° yields a peak at 128V which is not only more narrow than the centerline position but yields a most-probable energy that is higher than the centerline position. The 90° trace demonstrates a peak at 0V, but also contains a significant peak at 114V. These conflicting measurements could be attributed to pressure buildup within the RPA.

When ions make contact with the RPA collector, they induce a current by absorbing electrons from the collector surface. In this process, the ions recombine back into neutral propellant molecules. Without a means of venting from the RPA, these neutrals may build up within the probe and artificially increase the background pressure inside. In HET testing, where propellant may be accelerated directly into the RPA, pressure buildup of this nature is not uncommon. One way of combatting this is by moving the RPA outside of the plume for a few minutes in between traces. This gives the neutral particles ample time to vent from the probe in the reverse direction of entry. This was not performed, as it was not deemed an issue up until this point. RPA pressure buildup may lead to more elastic collisions inside the probe, distributing the influx of energy from the ions amongst a greater number of slow-moving particles. This could lead to the broadening of the peak and the reduction of the net most-probable energy. Pressure buildup typically occurs for high-flow HET configurations when the RPA is centerline with the thruster. This would explain why buildup was not prevalent in the 45° or 90° traces. Further, because the max T/P configuration outputs nearly twice as much propellant as the max I_{sp} configuration, this would explain why buildup did not occur in any of the previous traces either.

Given the above, we conclude that the centerline RPA trace for max T/P was subject to pressure buildup. We cannot ascertain an exact V_{RPA} value for this configuration. That being said, we do know that the most-probable voltage decreases as the probe is moved further from the centerline. Assuming that RPA pressure buildup was not an issue for the 45° position, and knowing that the most probable voltage for this position was 128 V, we assert that the true centerline V_{RPA} must be greater than this. Using this value, the voltage utilization efficiency for the max T/P configuration is greater than 85.4%.

IV. Discussion

The HET-X inputs for the max I_{sp} and max T/P configurations are summarized below in Table 1.

Table 1. *HET-X Inputs for max I_{sp} and T/P configs.*

Configuration	Max. I_{sp}	Max. T/P
Discharge Voltage [V]	340	150
Discharge Current [A]	1.88	3.84
Inner Magnet Voltage [V]	10.26	10.44
Inner Magnet Current [A]	2.53	2.53
Outer Magnet Voltage [V]	4.39	4.81
Outer Magnet Current [A]	0.88	0.88
HC Keeper Voltage [V]	26	20
HC Keeper Current [A]	0.2	0.2
Total Power [W]	674	611
Cathode-to-Ground [V]	-15.5	-15.0
Anode Flow [Xe mg/s]	2.44	3.90
Cathode Flow [Xe mg/s]	0.29	0.97
Facility Pressure [Torr]	1.0×10^{-6}	2.2×10^{-6}

The resulting performance metrics which were detailed above are tabulated below in Table 2. Generally, the HET-X thruster performs well. Despite being a thruster of new design and concept, the HET-X prototype boasts performance similar to those of other established HET developers.

Table 2. *HET-X performance for max I_{sp} and T/P configs.*

Configuration	Max. I_{sp}	Max. T/P
Thrust [mN]	37.8	42.8
Specific Impulse I_{sp} [s]	1576.0	1116.2
T/P Ratio [mN/kW]	56.0	70.2
Total Efficiency η [-]	38.7%	30.8%
Beam Efficiency η_b [-]	92.4%	89.5%
Divergence Efficiency η_d[-]	85.4%	80.0%
Volt. Util. Efficiency η_V [-]	93.6%	>85.4%

Based on the data collected from this campaign, we note that the divergence efficiency is relatively low and should be a target for improvement. Previous research has demonstrated that this may be done by increasing the discharge voltage [16]. However, the allowable V_D of this thruster is limited by the small-sat platform it is intended for. Thus, recommended modes of improvement might include alterations to the channel dimensions [17] and the propellant distributor [18].

The voltage, divergence, and beam efficiencies shown here represent three of the five factors that define total efficiency η. Because η is markedly lower than the η_v, η_d, and η_b, there is an implication that η_m or η_q may be considerably low. Thus, future research should investigate mass efficiency and charge utilization efficiency as possible sources of underperformance, and thus, modes of improvement. Future work should incorporate the ExB probe to measure mass utilization and charge efficiencies. It will also serve to refine the traces obtained by the Faraday and RPA probes. Measurements from these two probes should also be built upon, by collecting several traces of each and performing measurements at multiple background facility pressures.

Table 3. *Comparative HET Performance on Xenon [19]*

Manufacturer	Product	P (W)	T (mN)	I_{sp} (s)
Astra	ASE	400	25	1400
Busek	BHT-600	600	39	1495
EDB Fakel	SPT-70M	660	41	1580
EOI	HET-X (*max* I_{sp})	674	38	1576
EOI	HET-X (*max* T/P)	611	43	1116
Safran	PPS-X00	650	43	1530
SITAEL	HT400	615	28	1116

V. Conclusions

The Hall effect thruster prototype, HET-X, was operated, optimized, and characterized on xenon propellant. Optimal configurations for maximum I_{sp} and maximum T/P were identified. Thrust stand, discharge characteristics, and far-field probe measurements were used to measure total, beam, divergence, and voltage efficiency. The thruster has demonstrated performance characteristics that are comparable to those of similar sub-kW HETs built by other established developers. Divergence efficiency has been identified as a mode for improvement. Since HET-X has been proven effective on xenon, subsequent research should also consist of testing the thruster on a variety of other gases to verify its "propellant agnosticism." Gases under consideration include krypton, argon, nitrogen, oxygen, and atmospheric mixtures.

Acknowledgments

This publication was made possible by the research campaign sponsor, Earth Observant Inc. This author thanks them for permission to use their experimental data for academic purposes. This author also thanks Janice Cabrera, Maurice Boone, Taylor Hampson, and the rest of the support team at HPEPL for their help in test operations and data acquisition.

References

[1] Myers, R., and Carpenter, C., "High Power Solar Electric Propulsion for Human Space Exploration Architectures," presented at the IEPC 2011, 2011.

[2] Kieckhafer, A., and Walker, M., "Recirculating Liquid Nitrogen System for Operation of Cryogenic Pumps," presented at the IEPC 2011, 2011.

[3] Polk, J. E., Pancotti, A., Haag, T., King, S., Walker, M., Blakely, J., and Ziemer, J., "Recommended Practice for Thrust Measurement in Electric Propulsion Testing," *Journal of Propulsion and Power*, Vol. 33, No. 3, 2017, pp. 539–555. https://doi.org/10.2514/1.B35564

[4] Brown, D. L., Walker, M. L. R., Szabo, J., Huang, W., and Foster, J. E., "Recommended Practice for Use of Faraday Probes in Electric Propulsion Testing," *Journal of Propulsion and Power*, Vol. 33, No. 3, 2017, pp. 582–613. https://doi.org/10.2514/1.B35696

[5] McVey, J., Britt, E., Engelman, S., Gulczinski, F., Beiting, E., Pollard, J., and Cohen, R., "Characteristics of the T-220 HT Hall-Effect Thruster," presented at the 39th AIAA/ASME/SAE/ASEE Joint Propulsion Conference and Exhibit, Huntsville, Alabama, 2003. https://doi.org/10.2514/6.2003-5158

[6] Kamhawi, H., Huang, W., Haag, T., Yim, J., Herman, D., Peterson, P. Y., Williams, G., Gilland, J., Hofer, R., and Mikellides, I., "Performance, Facility Pressure Effects, and Stability Characterization Tests of NASA's Hall Effect Rocket with Magnetic Shielding Thruster."

[7] Brown, D. L., Blakely, J. M., and Lobbia, R. B., "Low-Voltage Hall Thruster Mode Transitions," presented at the 50th AIAA/ASME/SAE/ASEE Joint Propulsion Conference, Cleveland, OH, 2014. https://doi.org/10.2514/6.2014-3510

[8] Hofer, R. R., and Gallimore, A. D., "High-Specific Impulse Hall Thrusters, Part 2: Efficiency Analysis," *Journal of Propulsion and Power*, Vol. 22, No. 4, 2006, pp. 732–740. https://doi.org/10.2514/1.15954

[9] Huang, W., Shastry, R., Soulas, G. C., and Kamhawi, H., "Farfield Plume Measurement and Analysis on the NASA-300M and NASA-300MS," 2013.

[10] Trunec, D., "The Numerical Differentiation of Probe Characteristic," *Contributions to Plasma Physics*, Vol. 32, No. 5, 1992, pp. 523–534. https://doi.org/10.1002/ctpp.2150320505

[11] Hagstrum, H. D., "Auger Ejection of Electrons from Tungsten by Noble Gas Ions," *Physical Review*, Vol. 96, No. 2, 1954, pp. 325–335. https://doi.org/10.1103/PhysRev.96.325

[12] Kim, S.-W., and Gallimore, A. D., "Plume Study of a 1.35 kW SPT-100 Using an ExB Probe."

[13] Böhm, C., and Perrin, J., "Retarding-field Analyzer for Measurements of Ion Energy Distributions and Secondary Electron Emission Coefficients in Low-pressure Radio Frequency Discharges," *Review of Scientific Instruments*, Vol. 64, No. 1, 1993, pp. 31–44. https://doi.org/10.1063/1.1144398
[14] Conversano, R., Goebel, D. M., Hofer, R., Matlock, T., and Wirz, R. E., "Magnetically Shielded Miniature Hall Thruster: Development and Initial Testing," presented at the IEPC, 2013.
[15] Beal, B. E., and Gallimore, A. D., "Energy Analysis of a Hall Thruster Cluster," presented at the IEPC, 2003.
[16] Munro-O'Brien, T. F., and Ryan, C. N., "Performance of a Low Power Hall Effect Thruster with Several Gaseous Propellants," *Acta Astronautica*, Vol. 206, 2023, pp. 257–273. https://doi.org/10.1016/j.actaastro.2023.01.033
[17] Raitses, Y., Ashkenazy, J., and Guelman, M., "Propellant Utilization in Hall Thrusters," *Journal of Propulsion and Power*, Vol. 14, No. 2, 1998, pp. 247–253. https://doi.org/10.2514/2.5274
[18] Fan, H., Ding, Y., Wang, L., Chen, Z., Zhang, Y., Wei, L., Li, H., and Yu, D., "Effects of Gas Supply Direction on the Discharge Characteristics of a Low-Power Hall Thruster," *Vacuum*, Vol. 174, 2020, p. 109193. https://doi.org/10.1016/j.vacuum.2020.109193
[19] "State-of-the-Art Small Spacecraft Technology 2022," Small Spacecraft Systems Virtual Institute, 2022.